

Anisotropic microplane constitutive model for coupling creep and damage in layered geomaterials such as gas or oil shale



Cunbao Li^{a,b,c,*}, Zdeněk P. Bažant^d, Heping Xie^{a,c}, Saeed Rahimi-Aghdam^d

^a Institute of Deep Earth Sciences and Green Energy, Shenzhen University, China

^b Institute of New Energy and Low-Carbon Technology, Sichuan University, China

^c MOE Key Laboratory of Deep Underground Science and Engineering, Sichuan University, China

^d Department of Civil and Environmental Engineering, Northwestern University, USA

ARTICLE INFO

Keywords:

Anisotropic microplane model
Anisotropic time-dependent material behavior
Damage evolution
Viscoelasticity
Kelvin chain
Retardation spectrum
Hydraulic fracturing of shale

ABSTRACT

An anisotropic constitutive model for coupling creep with damage of shale and other anisotropic geomaterials under complex loading paths is formulated. The material damage is described by a previously developed spherocylindrical microplane model, which can simulate not only the stress-induced incremental anisotropy but also the inherent material anisotropy. Like material damage, the creep must be expected to be anisotropic as well. The creep responses of shale with inherent transverse isotropy are first separately constructed for the loading by compressive principal stress oriented either (i) parallel or (ii) normal to the bedding planes, and (iii) for shear stress along the bedding planes produced by the differences of the bedding plane inclination angle. This leads to three elementary linear creep models, which are mathematically formulated based on a continuous retardation spectrum of generalized Kelvin chain. These three creep responses are combined with the spherocylindrical microplane model. This leads to a general anisotropic constitutive creep model for arbitrary three-dimensional applied loading and arbitrary loading path. To achieve high numerical efficiency, a fully explicit numerical algorithm for the microplane constitutive model and finite element analysis is then formulated. Short-time (two-day) creep tests of shale cylinders with multilevel deviatoric stress and various inclinations of bedding planes relative to the axial compressive load are conducted. The numerical simulations by the microplane model are compared with the results of laboratory creep tests. The comparisons demonstrate a linear dependence of creep on the stress and verify the applicability of the anisotropic microplane model for creep and damage. Extensions to multi-year time ranges are in principle possible but will necessitate further calibration and verification.

1. Introduction

The astonishing success of horizontal drilling and hydraulic fracturing (aka fracking, or frac) have enabled commercialized production of methane from low-permeability reservoirs, such as shale.¹ However, a significant decline in the shale gas production rate from deep shale-gas reservoirs occurs after the initial hydraulic fracturing treatment. For the Woodford, Eagleford, Barnett, Fayetteville and Haynesville shale gas reservoirs, the average decrease in productivity rates during the first 3 years ranges from 77% to 89%. Most field data reveal that the production rates generally decrease by 45%–55% after the first 5–6 months after hydraulic fracturing.² The decline has various causes. The main one doubtless is a slowing gas diffusion from shale nanopores into the hydraulic cracks.³ An additional cause, however, may be the growth of embedment of proppant (i.e., sand) grains into crack walls due to

creep and hydration of shale, which makes the hydraulic fractures narrower.^{4–6} Another cause maybe that some segments of hydraulic cracks may be penetrated by proppant incompletely or not at all, which leads to crack closing. Furthermore, creep affects the rate of growth of hydraulic cracks.⁷ Understanding of these creep phenomena and mechanisms of shale is important for extraction of shale gas or oil.

The creep and generally the time-dependent inelastic deformation of anisotropic rock has been studied experimentally in various laboratories. For example, Sone⁸ conducted a series of triaxial tests on shale samples to study the influence of clay content. His results indicated that the higher the clay content, the larger the creep. The creep strain was found to be higher for compression parallel, rather than normal, to the bedding planes.^{8–10} Hence, the creep of shale is anisotropic or, more precisely, transversely isotropic. Anisotropic creep is also observed in other anisotropic rocks, such as clayey rocks,¹¹ mica schist,¹² and

* Corresponding author. Institute of Deep Earth Sciences and Green Energy, Shenzhen University, China.

E-mail addresses: cunbao.li@scu.edu.cn, cunbao.li@hotmail.com (C. Li).

argillite.¹³ However, in most published creep tests, the bedding plane orientation, which is defined in Fig. (5), is either 0° or 90°. Information on anisotropic creep is scant.

Most existing creep models for shale are limited to a simple power law or log-power law describing the experimental creep curve.^{9,14,15} To generalize these laws to more complex loading, rheological models consisting of Newtonian dashpots and Heookean springs have been proposed to describe viscoelastic or viscoelastic-plastic behavior of isotropic rock.^{12,16–18} To consider the effects of damage, a damage factor has been introduced to modify the spring or dashpot properties and thus obtain a nonlinear creep model.^{19,20} However, none of these models considered creep anisotropy theoretically, and none are applicable to compression loading at an oblique angle with the bedding planes.

Some researchers^{21–23} attempted to couple the creep and damage in the framework of continuous damage mechanics or irreversible thermodynamics with internal variables, although not associated with a specific orientation. The use of tensor formalism in damage mechanics has not allowed capturing the directional damage induced by frictional slip and microcracking. For example, in these tensor-based damage models, the internal friction is generally characterized by introducing a relation between the first stress invariant and the second deviatoric stress invariant. However, this method cannot capture the fact that frictional slips occur only along cracks of certain distinct orientations. These models cannot be trusted to represent the creep of anisotropic shale under different or nonproportional loading paths, with varying inclination of loading.

The purpose of this work is to develop a general anisotropic model for creep and damage in shale and other rocks, applicable to loading of arbitrary orientation. Only the special case of orthotropy, characteristic of layered microstructures, will be considered.

2. A brief description of spherocylindrical microplane theory for anisotropic geomaterials

2.1. Framework of spherocylindrical microplane theory

The microplane constitutive theory was originally proposed for simulating the progressive damage of quasibrittle materials such as concrete^{25–30} and other materials.^{31,32} The microplane model not only captures incremental stress-induced anisotropy, but also the structural, or inherent, material anisotropy, which already exists in the initial state of the material. As in all nonlinear constitutive models, the coupling between the inherent and stress-induced material anisotropy is has been a major challenge.^{33,34}

In the framework of microplane theory, various methods have been used to capture the coupled anisotropy: 1) The dependence of microplane stiffness parameters on the orientation angle θ (Fig. 1) of the microplane,^{35–38} which, however, proved insufficient for strong orthotropy of composites³⁹; 2) the spectral stiffness microplane model,³⁹ whose approach to orthotropy is fully general and works well for the elasticity and fracturing of woven composite laminates,⁴⁰ but is difficult and not intuitive for data fitting; and 3) the microplane triad model,⁴¹ which is specific to the textile composites and has been developed to derive orthotropic elastic constants and fracturing behavior from the yarn architecture.

For shale, however, all these methods have appeared ineffective. Adopted here is a recently formulated approach, called the spherocylindrical microplane model,²⁴ which can capture this non-monotonicity and describe the inherent transverse isotropy of shale with damage. This model consists of two microplane systems, i.e., one spherical system and one cylindrical system. The systems are here called the *phases* (Fig. 1).

In the spherocylindrical microplane configuration, it is assumed that the classical spherical phase is coupled with the cylindrical phase in parallel. i.e., the strain tensors ε_{ij} (with $i, j = 1, 2, 3$) in the spherical and

cylindrical phases are the same. The strain vectors on the microplanes of both phases are calculated from the projections of the strain tensor. The stress vectors on the microplanes, calculated from the strain vectors based on the constitutive law, are used to obtain the macroscale stress tensor in each phase based on the virtual work principle. Then, the macroscopic stress σ_{ij} of the spherocylindrical model is computed by superposing the stress tensors obtained from the spherical phase and cylindrical phase on the basis of the partition of unity, i.e., these tensors are weighted as $\alpha\sigma_{ij}$ and $(1 - \alpha)\sigma_{ij}$, respectively, where α represents volumetric proportion of the spherical microplane system.

The strain vectors $\vec{\varepsilon}_N^s$ (Fig. 1(b)) and $\vec{\varepsilon}_N^c$ (Fig. 1(c)) on the microplanes of the spherical and cylindrical phases are calculated on the basis of the kinematic constraint,³⁰ i.e.,

$$\varepsilon_{Ni}^s = \varepsilon_{ij} n_j^s, \quad \varepsilon_{Ni}^c = \varepsilon_{ij} n_j^c \quad (1)$$

where n_j^s and n_j^c are the unit normal vectors components of the spherical microplane and cylindrical microplane, respectively.

Then the strain vector components on each microplane are computed as follows:

$$\varepsilon_N^s = \varepsilon_{ij} N_{ij}^s, \quad \varepsilon_L^s = \varepsilon_{ij} L_{ij}^s, \quad \varepsilon_M^s = \varepsilon_{ij} M_{ij}^s \quad (2)$$

$$\varepsilon_N^c = \varepsilon_{ij} N_{ij}^c, \quad \varepsilon_L^c = \varepsilon_{ij} L_{ij}^c, \quad \varepsilon_M^c = \varepsilon_{ij} M_{ij}^c \quad (3)$$

where

$$N_{ij}^s = n_i^s n_j^s, \quad L_{ij}^s = (l_i^s n_j^s + l_j^s n_i^s)/2, \quad M_{ij}^s = (m_i^s n_j^s + m_j^s n_i^s)/2 \quad (4)$$

$$N_{ij}^c = n_i^c n_j^c, \quad L_{ij}^c = (l_i^c n_j^c + l_j^c n_i^c)/2, \quad M_{ij}^c = (m_i^c n_j^c + m_j^c n_i^c)/2 \quad (5)$$

Here, l_i^s , m_i^s , l_i^c and m_i^c are the unit tangential vector components' (\mathbf{l}^s , \mathbf{l}^c and \mathbf{m}^c). The vector \mathbf{n}^s defines the orientation of the spherical microplane. The vector is an arbitrary in-plane tangential unit vector, while the vector \mathbf{l}^s is calculated as $\mathbf{l}^s = \mathbf{m}^s \times \mathbf{n}^s$. Vector \mathbf{m}^c is fixed and is chosen to be normal to the axes x_1^c and x_2^c , i.e., $\mathbf{m}^c = (0, 0, 1)$, and then \mathbf{l}^c is determined by $\mathbf{m}^c \times \mathbf{n}^c$.

In the microplane theory, it was demonstrated that, in general, a realistic simulation of the inelastic mechanical characteristics of materials in the uniaxial or triaxial compression as well as tension requires decomposing the spherical microplane normal strain into its volumetric, ε_V , and deviatoric, ε_D^s , strain components; i.e.,

$$\varepsilon_D^s = \varepsilon_N^s - \varepsilon_V, \quad \varepsilon_V = \varepsilon_{ii}/3 \quad (6)$$

Generally, the stress vector on each microplane is determined by the microplane constitutive relationship. Then, the macroscopic stress tensor is calculated from microplane stress vectors based on the virtual work principle, i.e.,

$$\begin{aligned} \sigma_{ij} = & \alpha \frac{3}{2\pi} \int_{\Omega} (\sigma_N^s N_{ij}^s + \sigma_L^s L_{ij}^s + \sigma_M^s M_{ij}^s) d\Omega \\ & + (1 - \alpha) \frac{1}{\pi} \int_S (\sigma_N^c N_{ij}^c + \sigma_L^c L_{ij}^c + \sigma_M^c M_{ij}^c) dS \end{aligned} \quad (7)$$

where, Ω is the unit hemispherical surface; S is the unit cylindrical surface; and σ_N^s , σ_L^s , σ_M^s , σ_N^c , σ_L^c and σ_M^c are the stress vector components on the microplanes of the spherical and cylindrical phases.

2.2. Constitutive characterization of elastic and inelastic behaviors of anisotropic geomaterials

Different spherical and cylindrical microplanes with diverse orientations can be in loading or unloading stages at the same time. Also, different microplanes undergo elastic or inelastic deformations stages at diverse times during the loading and unloading, which accounts for the gradual formation of microcracks or frictional dilatant microslips during the deformation process. At the microplane level, there are many random assortments of such loading, reloading and unloading on the microplanes with different orientations, which is next to impossible to capture using phenomenological tensorial models. Therefore, even

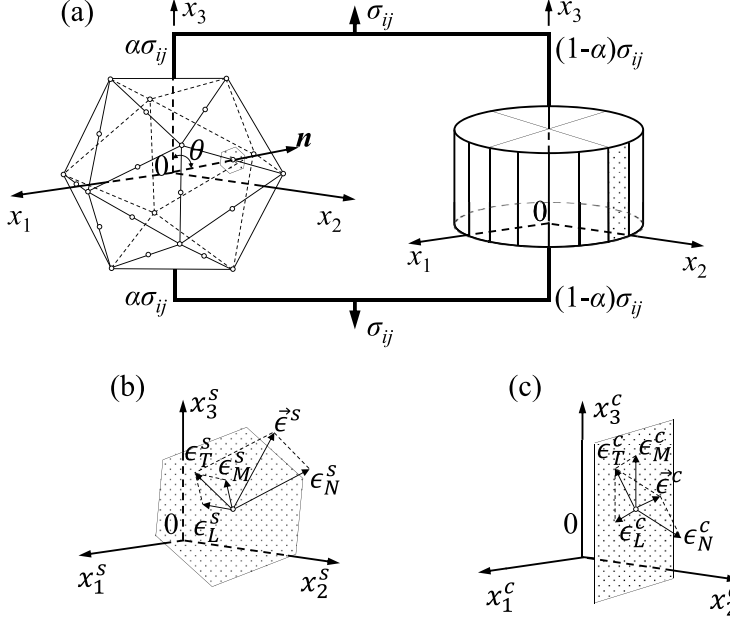


Fig. 1. (a) Diagram of the spherocylindrical microplane system; (b) strain vector on one spherical microplane; (c) strain vector on one cylindrical microplane.

though the constitutive relationship on the microplane is considered to be path-independent, the macroscopic response of the material can exhibit considerable path dependence. It can thus be assumed that the stress-strain response on the microplane is independent of the loading path under the condition that this microplane monotonic loading. The consequence of this assumption is that the elastic constants on the microplane can be calculated from the current stress vector and strain vector only. Furthermore, the modeling experience indicates that strain and stress components on each microplane can be considered to be independent of each other. The interdependence of stress and strain components on planes of different orientations is introduced on a higher level through the kinematic constraint.

Thus, the stress-strain relations on the microplane can be decoupled and simply defined as follows:

$$\sigma_V = E_V \epsilon_V, \sigma_N^S = E_N^S \epsilon_N^S, \sigma_D^S = E_D^S \epsilon_D^S, \sigma_M^S = E_M^S \epsilon_M^S, \sigma_L^S = E_L^S \epsilon_L^S, \quad (8)$$

$$\sigma_N^C = E_N^C \epsilon_N^C, \sigma_L^C = E_L^C \epsilon_L^C, \sigma_M^C = E_M^C \epsilon_M^C \quad (9)$$

where \$E_V\$, \$E_N^S\$, \$E_D^S\$, \$E_L^S\$, \$E_M^S\$, \$E_N^C\$, \$E_L^C\$, \$E_M^C\$ are the material parameters of the spherical and cylindrical microplanes. All those elastic parameters are constant before reaching the strength limit irrespective of the microplane orientation.

By substituting Eq. (8) and Eq. (9) into Eq. (7), the macroscopic stiffness \$\bar{C}_{ijkl}\$ can be computed as follows:

$$\begin{aligned} \bar{C}_{ijkl} &= \alpha \frac{3}{2\pi} \int_{\Omega} \left(E_D^S N_{ij}^S N_{kl}^S + \frac{1}{3}(E_V - E_D^S) N_{ij}^S \delta_{kl} + E_L^S L_{ij}^S L_{kl}^S + E_M^S M_{ij}^S M_{kl}^S \right) d\Omega \\ &\quad + (1-\alpha) \frac{1}{\pi} \int (E_N^C N_{ij}^C N_{kl}^C + E_L^C L_{ij}^C L_{kl}^C + E_M^C M_{ij}^C M_{kl}^C) d\Omega \end{aligned} \quad (10)$$

By comparing the corresponding components on both sides of Eq. (10), one can obtain the elastic parameters on the microplane using the following equations²⁴:

$$E_V = (C_{33} + 2C_{13})/\alpha \quad (11)$$

$$E_L^S = E_M^S = E_T^S = (C_{33} - C_{13})/\alpha \quad (12)$$

$$E_D^S = (C_{33} - C_{13})/\alpha \quad (13)$$

$$E_N^C = 2(C_{11} - C_{33} + C_{12} - C_{13})/(1 - \alpha) \quad (14)$$

$$E_L^C = 2(C_{11} - C_{33} - 3C_{12} + 3C_{13})/(1 - \alpha) \quad (15)$$

$$E_M^C = 4(2C_{44} - C_{33} + C_{13})/(1 - \alpha) \quad (16)$$

Here \$C_{11}\$, \$C_{12}\$, \$C_{13}\$, \$C_{33}\$ and \$C_{44}\$ are the five independent elements of the elastic stiffness matrix \$C_{ij}\$ of shale.

Assuming \$\Delta\epsilon_V\$, \$\Delta\epsilon_D^S\$, \$\Delta\epsilon_L^S\$, \$\Delta\epsilon_M^S\$, \$\Delta\epsilon_N^S\$, and \$\Delta\epsilon_L^C\$ are the strain increments on the microplanes in one load step, then the elastic stress vector components on the spherical and cylindrical microplane at the end of the load step can be computed as follows:

$$\sigma_V = \sigma_V^{(0)} + E_V \Delta\epsilon_V \quad (17)$$

$$\sigma_D^S = \sigma_D^S^{(0)} + E_D^S \Delta\epsilon_D^S \quad (18)$$

$$\sigma_L^S = \sigma_L^S^{(0)} + E_L^S \Delta\epsilon_L^S \quad (19)$$

$$\sigma_M^S = \sigma_M^S^{(0)} + E_M^S \Delta\epsilon_M^S \quad (20)$$

$$\sigma_N^C = \sigma_N^C^{(0)} + E_N^C \Delta\epsilon_N^C \quad (21)$$

$$\sigma_L^C = \sigma_L^C^{(0)} + E_L^C \Delta\epsilon_L^C \quad (22)$$

$$\sigma_M^C = \sigma_M^C^{(0)} + E_M^C \Delta\epsilon_M^C \quad (23)$$

Here the superscript (0) refers to the initial stress vector component at the beginning of the load step. Based on the foregoing formulae, the elastic behavior of shale can be fully described.

The anisotropic inelastic deformation of shale can be depicted by the strain-dependent strength limit on each microplane, which was proposed by Bažant and referred to as stress-strain boundaries.²⁷ The anisotropic deformation is elastic within the boundary. If the stress exceeds the boundary in one load step, then it is returned to the boundary while the strain is kept constant (which is a special case of the well-known radial return algorithm for tensorial models). Despite the abrupt change in slope of the stress vector components when the boundaries are exceeded, the macroscopic deformation is quite smooth because microplanes with different orientations enter the loading or unloading stage and reach the boundary at different times and loading

steps. For each stress vector component on one microplane, the corresponding boundary can be described by functions of the corresponding strain vector component.

Thus, the stress-strain boundary for each stress vector component on the spherical microplane can be defined as

$$\sigma_N^{sb+} = F_N^s(\varepsilon_N^s, \varepsilon_V), \quad \sigma_D^{sb+} = F_D^s(\varepsilon_D^s), \quad \sigma_D^{sb-} = F_D^s(-\varepsilon_D^s), \quad \sigma_T^{sb} = F_T^s(\sigma_N^s) \quad (24)$$

where

$$\sigma_T^s = \sqrt{(\sigma_L^s)^2 + (\sigma_M^s)^2} \quad (25)$$

In similarity to the spherical boundaries, the stress-strain boundary for each cylindrical stress vector component is defined as

$$\sigma_N^{cb+} = F_N^c(\varepsilon_N^c, \varepsilon_V), \quad \sigma_D^{cb+} = F_D^c(-\varepsilon_N^c, \varepsilon_V), \quad \sigma_T^{cb} = F_T^c(\sigma_N^c) \quad (26)$$

where

$$\sigma_T^c = \sqrt{(\sigma_L^c)^2 + (\sigma_M^c)^2} \quad (27)$$

The microplane system is what makes it possible to capture the anisotropy of progressive deformation, including the effects of the inherent transverse isotropy and of the stress-induced anisotropic damage. For a further description of the inelastic behavior of the spherocylindrical microplane model, see [24].

3. Transversely isotropic creep behavior

3.1. Three different patterns of creep of transversely isotropic shale

Due to the presence of bedding planes, the mechanical characteristics of shale vary significantly with the inclination angle of the compressive load from the normal of the bedding planes. In terms of principal stresses, the stress tensor σ'_{ij} of the representative volume element of shale in the global coordinate system (x' , y' , z') (Fig. 2) is written as

$$\sigma'_{ij} = \begin{bmatrix} \sigma'_{x'x'} & 0 & 0 \\ 0 & \sigma'_{y'y'} & 0 \\ 0 & 0 & \sigma'_{z'z'} \end{bmatrix} \quad (28)$$

where $i, j = x', y', z' =$ Cartesian subscripts.

The bedding planes are what causes the shale to be a transversely isotropic material. In general, one needs to describe the mechanical properties of shale in terms of the material coordinate system (x , y , z) where z is normal to the bedding planes; see Fig. 2. Based on the coordinate transformation rules, the principal stress tensor σ' with elements σ'_{ij} , defined in Eq. (28) in the material coordinate system (x , y , z), is written as

$$\sigma_{ij} = M_{ik} \sigma'_{kl} M_{lj} \text{ or } M^T \sigma' M \quad (29)$$

where superscript T denotes a matrix transpose and M_{ij} are the elements

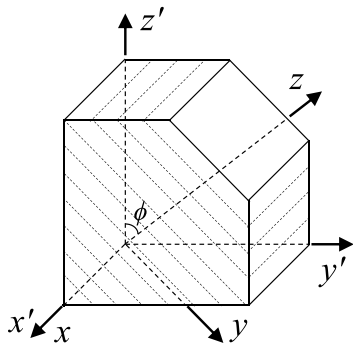


Fig. 2. Schematic diagram of coordinates transformation for transverse isotropy.

of the coordinate rotation matrix M , which read

$$M_{ij} = \begin{bmatrix} 1 & 0 & 0 \\ 0 & \cos \phi & \sin \phi \\ 0 & -\sin \phi & \cos \phi \end{bmatrix} \quad (30)$$

Here, ϕ is the angle of rotation of the local coordinate system around the x axis, as shown in Fig. 2. Therefore, σ_{ij} may be rewritten as

$$\sigma_{ij} = \begin{bmatrix} \sigma'_{x'x'} & 0 & 0 \\ 0 & \sigma'_{y'y'} \cos^2 \phi + \sigma'_{z'z'} & \sigma'_{y'y'} \sin \phi \cos \phi - \sigma'_{z'z'} \sin \phi \cos \phi \\ 0 & \sin^2 \phi & \sigma'_{z'z'} \\ 0 & \sigma'_{y'y'} \sin \phi \cos \phi - \sigma'_{z'z'} & \sigma'_{y'y'} \sin^2 \phi + \sigma'_{z'z'} \cos^2 \phi \\ 0 & \sin \phi \cos \phi & \end{bmatrix} \quad (31)$$

The bedding planes complicate the response to the stress tensor σ_{ij} components. For the in-plane x and y directions, the stiffness is stronger than for the transverse z direction; thus, e.g., when $\sigma_{xx} = \sigma_{yy} = \sigma_{zz}$, the creep in the z direction will be smaller. The bedding layer planes are the planes of weakness, and both their deformation resistance and strength are quite small. If shear stress σ_{yz} acts on the bedding plane, the shear creep strain will be larger than on the other planes.

Three elementary configurations of principal stresses applied on shale specimens with bedding layers of different orientations are considered in this study, as shown in Fig. 3. The first and second elementary loading configurations consist of a stress component applied in the direction parallel and normal to the bedding layers, respectively. In the third configuration, the bedding layers are inclined relative to the principal stress directions, and the principal stress difference produces shear stress loading along the bedding layers (Fig. 3). Each of these stress configurations leads to different creep responses.

For the creep of shale under general three-dimensional loading conditions, the anisotropic creep mechanism and deformation can be treated as a combination of these three elementary configurations. Each elementary configuration can be described by a Kelvin chain model with a continuous retardation spectrum, as presented next.

3.2. Creep compliance based on a Kelvin chain model and continuous retardation spectrum

Viscoelastic creep occurs in undamaged shale, which is the shale between the cracks, while fracturing (or damage) strain is the continuum smearing of deformations in the cracks. Therefore, the creep strain is additive to the fracturing strain. Based on the existing limited test data, the creep law of shale seems to be linear in stress, approximately adhering to the principle of superposition, and can be effectively modeled using the Kelvin chain model (Fig. 4 (a)).⁴⁷ The compliance function $J(t)$ can be written as

$$J(t) = \frac{1}{E_0} + C(t) \quad (32)$$

where E_0 represents the asymptotic elastic modulus when the loading duration is extremely short and $C(t)$ is the creep compliance function, which is written as

$$C(t) = \sum_{\mu=1}^K \frac{1}{E_\mu} (1 - e^{-t/\tau_\mu}) \quad (33)$$

Here M is the total number of Kelvin units, E_μ is the spring modulus of the μ^{th} Kelvin unit, and τ_μ is the retardation time, which is defined as

$$\tau_\mu = \frac{\eta_\mu}{E_\mu} \quad (34)$$

where η_μ is the viscosity parameter of the dashpot in the μ^{th} Kelvin unit.

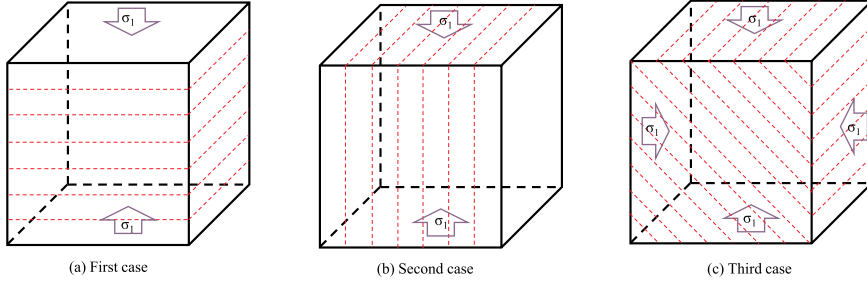


Fig. 3. Three elementary creep configurations for creep of transversely isotropic material to be combined in the general constitutive model.

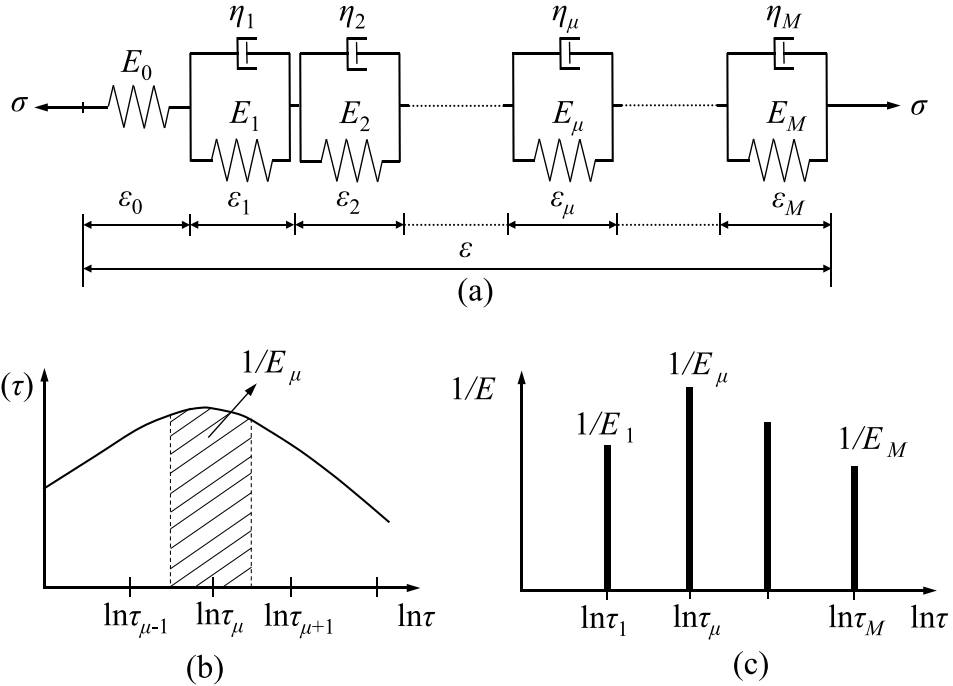


Fig. 4. (a) Kelvin chain creep model; (b) continuous retardation spectrum; (c) discrete retardation spectrum.

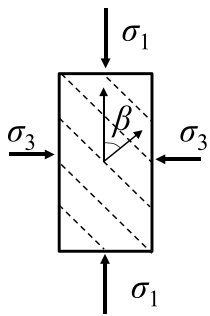


Fig. 5. Schematic of the bedding layer orientation (β), which is defined as the angle between the normal direction of the bedding plane and the axial loading direction.

$1/E_\mu$ as functions of τ define a discrete retardation spectrum. But it is convenient to introduce a continuous approximation of Eq. (33), representing a continuous retardation spectrum (Fig. 4 (b)). It is

defined as

$$C(t) = \int_0^t \frac{1}{E_\mu} (1 - \exp^{-t'/\tau_\mu}) d(t') \quad (35)$$

In the creep models^{44–46} based on the discrete retardation time spectrum (Eq. (33) and Fig. 4 (c)), all the spring moduli for a set of chosen τ_μ -values have to be calibrated by fitting the experimental creep curve. As is well known, the τ_μ values cannot be identified from the test data uniquely because their calculation is an ill-posed problem. They need to be chosen such that they cover the time range of interest completely and sufficiently densely but not too densely, to avoid ill-posedness (spacing by decades is generally best). To prevent it, it is better use a continuous retardation spectrum,^{47–49} from which the Kelvin unit stiffnesses, spring moduli and dashpot viscosities can be calculated.

Eq. (35) can be reformulated in a continuous form,

$$C(t) = \int_{-\infty}^{\infty} L(\tau) (1 - \exp^{-t/\tau}) d(\ln \tau) \quad (36)$$

where $L(\tau)$ is the definition of continuous retardation spectrum (Fig. 4 b).

Based on the Laplace transform theory, a good approximation of $L(\tau)$ is obtained from Widders' formula⁴⁹:

$$L(\tau) = -\lim_{k \rightarrow \infty} \frac{(-k\tau)^k}{(k-1)!} C^{(k)}(k\tau) \quad (37)$$

where $C^{(k)}$ is the k^{th} derivative of $C(t)$. Normally, it suffices to use derivatives only up to the third. For the purpose of numerical calculations, one may then use a finite sum (Fig. 4 c):

$$C(t) = \sum_{\mu=1}^K L(\tau_\mu) (1 - \exp^{-t/\tau_\mu}) \ln 10 \Delta(\log \tau_\mu) \quad (38)$$

Here, as usual, the retardation times τ_μ are selected to form a geometric progression with quotient 10, covering the entire time range of interest. The time integration requires the exponential algorithm,^{43,47} which is unconditionally stable.

Then, the elastic modulus and viscosity of the Kelvin unit can be computed as

$$E_\mu(t) = 1/[L(\tau_\mu) \ln 10 \Delta(\log \tau_\mu)] \quad (39)$$

$$\eta_\mu(t) = \tau_\mu E_\mu(t) \quad (40)$$

Based on creep testing of shale, e.g., Refs.^{9,14,15} the creep compliance function $C(t)$ can be chosen to be a power-law function of time, i.e.,

$$C(t) = J_1 + B t^n \quad (41)$$

where J_1 is the asymptotic instantaneous compliance; B and n are material parameters. A power law is a logical choice since it is self-similar and no characteristic creep time is known. Substituting Eq. (41) into Eqs. 39 and 40, one can obtain the values of the elastic modulus and viscosity for each Kelvin unit, and then the creep deformation of each Kelvin unit can be calculated, as described in the following section.

3.3. Calculation of creep deformation under a three-dimensional stress field based on the generalized Kelvin chain model

3.3.1. Creep deformation calculation for one stress component

Consider a small time step for t_n to t_{n+1} , i.e., $\Delta t = t_{n+1} - t_n$, and denote the stress increment as $\Delta\sigma = \sigma(t_{n+1}) - \sigma(t_n)$. Based on the creep compliance obtained using the Kelvin chain model introduced in Section 3.2, the total three-dimensional strain increments in time step Δt under uniaxial stress can be computed as follows^{47,50}:

$$\Delta\varepsilon = \sum_{\mu=0}^K \Delta\varepsilon_\mu = \mathbf{C} \Delta\sigma \left(\frac{1}{E_0^{(n+1/2)}} + \sum_{\mu=1}^K \frac{1 - \lambda_\mu}{E_\mu^{(n+1/2)}} \right) + \sum_{\mu=0}^K (1 - \beta_\mu) \gamma_\mu^{(n)} \quad (42)$$

and

$$\gamma_\mu^{(n+1)} = \gamma_\mu(t_{n+1}) = \frac{\lambda_\mu}{E_\mu^{(n+1/2)}} \mathbf{D} (\Delta\varepsilon - \Delta\varepsilon'') \bar{E} + \beta_\mu \gamma_\mu^{(n)} \quad (43)$$

Here, $E_0^{(n+1/2)}$ represents the effective stiffness of the separate spring in the generalized Kelvin chain at the middle of time step Δt , i.e., $E_0^{(n+1/2)} = E_0(t_n + \Delta t/2)$. The variation of E_0 is caused by material damage, which is calculated using the spherocylindrical microplane model. Similarly, $E_\mu^{(n+1/2)}$ is $E_\mu(t_n + \Delta t/2)$; \mathbf{C} is a dimensionless 6×6 compliance matrix (involving the elastic moduli and Poisson ratios); ε is the 6×1 matrix of strains; $\gamma_\mu^{(n)}$ is the internal variable of the μ^{th} Kelvin unit at time t_n ; \mathbf{D} is the 6×6 inverse matrix of \mathbf{C} (dimensionless); $\Delta\varepsilon''$ is defined in Eq. (46); and β_μ and λ_μ are defined as follows:

$$\beta_\mu = e^{-\Delta t/\tau_\mu}, \lambda_\mu = \frac{\tau_\mu}{\Delta t} (1 - \beta_\mu) \quad (44)$$

The first part on the right-hand side of Eq. (42) can be regarded as

the strain increase induced by variation of the applied stress and material damage. The component in brackets of this part can be interpreted as the effective compliance under the effect of creep and damage, i.e.,

$$\frac{1}{\bar{E}} = \frac{1}{E_0^{(n+1/2)}} + \sum_{\mu=1}^K \frac{1 - \lambda_\mu}{E_\mu^{(n+1/2)}} \quad (45)$$

The second part on the right side of Eq. (42) refers to the strain increase induced by the creep deformation under constant stress condition, denoted as

$$\Delta\varepsilon'' = \sum_{\mu=1}^K (1 - \beta_\mu) \gamma_\mu^{(n)} \quad (46)$$

The equations presented so far give the creep and its effective compliance for only one macroscopic stress component. Generalization to macroscopic three-dimensional stress tensor follows.

3.3.2. Calculation of creep induced by three-dimensional stress tensor

Based on the three elementary creep patterns explained in Section 3.1, the creep deformation of shale under a general three-dimensional stress tensor can be calculated by superposing the strains produced by different stress components. According to the methodology in Section 3.3.1, the three-dimensional creep strain under different individual stress components can be written directly as follows:

(1). Creep deformation for stress σ_{zz}

The equation for calculating creep deformation is

$$\Delta\varepsilon_z = \mathbf{C}_z \Delta\sigma_{zz} \left(\frac{1}{E_{z(0)}^{(n+1/2)}} + \sum_{(\mu)=1}^K \frac{1 - \lambda_{(\mu)}}{E_{z(\mu)}^{(n+1/2)}} \right) + \sum_{\mu=0}^K (1 - \beta_{(\mu)}) \gamma_{z(\mu)}^{(n)} \quad (47)$$

where the subscript z represents the variable in this loading path, subscript (0) represents the initial value of the stiffness parameter, and subscript (μ) represents the μ^{th} Kelvin unit; the following notation is marked in the same manner. The updates of the internal variable and effective compliance are

$$\gamma_{z(\mu)}^{(n+1)} = \frac{\lambda_{(\mu)}}{E_{z(\mu)}^{(n+1/2)}} \mathbf{D}_z (\Delta\varepsilon_{zz} - \Delta\varepsilon_{zz}'') \bar{E}_z + \beta_{(\mu)} \gamma_{z(\mu)}^{(n)} \quad (48)$$

$$\frac{1}{\bar{E}_z} = \frac{1}{E_{z(0)}^{(n+1/2)}} + \sum_{(\mu)=1}^K \frac{1 - \lambda_{(\mu)}}{E_{z(\mu)}^{(n+1/2)}} \quad (49)$$

(2). Creep deformation for the stress σ_{yy}

The equation for calculating creep deformation is

$$\Delta\varepsilon_y = \mathbf{C}_y \Delta\sigma_{yy} \left(\frac{1}{E_{y(0)}^{(n+1/2)}} + \sum_{(\mu)=1}^K \frac{1 - \lambda_{(\mu)}}{E_{y(\mu)}^{(n+1/2)}} \right) + \sum_{\mu=0}^K (1 - \beta_{(\mu)}) \gamma_{y(\mu)}^{(n)} \quad (50)$$

where subscript y represents the variable in this loading path. The updates of the internal variable and effective compliance are

$$\gamma_{y(\mu)}^{(n+1)} = \frac{\lambda_{(\mu)}}{E_{y(\mu)}^{(n+1/2)}} \mathbf{D}_y (\Delta\varepsilon_{yy} - \Delta\varepsilon_{yy}'') \bar{E}_y + \beta_{(\mu)} \gamma_{y(\mu)}^{(n)} \quad (51)$$

$$\frac{1}{\bar{E}_y} = \frac{1}{E_{y(0)}^{(n+1/2)}} + \sum_{(\mu)=1}^K \frac{1 - \lambda_{(\mu)}}{E_{y(\mu)}^{(n+1/2)}} \quad (52)$$

(3). Creep deformation for stress σ_{xx}

Since the stiffnesses in the x direction and y direction are equal, the equations for calculating the creep deformation and updating the effective compliance are the same as applying stress σ_{yy} . However, the equation for updating the internal variable $\gamma_{y(\mu)}^{(n+1)}$ should use $\Delta\varepsilon_{xx}$ and $\Delta\varepsilon_{xx}''$ rather than $\Delta\varepsilon_{yy}$ and $\Delta\varepsilon_{yy}''$, and so it is written as

$$\gamma_{y(\mu)}^{(n+1)} = \frac{\lambda_{(\mu)}}{E_{y(\mu)}^{(n+1/2)}} \mathbf{D}_y (\Delta\varepsilon_{xx} - \Delta\varepsilon_{xx}'') \bar{E}_y + \beta_{(\mu)} \gamma_{y(\mu)}^{(n)} \quad (53)$$

(4). Creep deformation for stress σ_{xy}

The equation for calculating the creep deformation is

$$\Delta\epsilon_{xy} = C_{xy}\Delta\sigma_{xy}\left(\frac{1}{E_{xy(0)}^{(n+1/2)}} + \sum_{(\mu)=1}^K \frac{1-\lambda_{(\mu)}}{E_{xy(\mu)}^{(n+1/2)}}\right) + \sum_{(\mu)=0}^K (1-\beta_{(\mu)})\gamma_{xy(\mu)}^{(n)} \quad (54)$$

where the subscript xy refers to the variable for this loading path. The updates of the internal variable and effective compliance are

$$\gamma_{xy(\mu)}^{(n+1)} = \frac{\lambda_{(\mu)}}{E_{xy(\mu)}^{(n+1/2)}} D_{xy}(\Delta\epsilon_{yy} - \Delta\epsilon_{yy}'') \bar{E}_{xy} + \beta_{(\mu)} \gamma_{xy(\mu)}^{(n)} \quad (55)$$

$$\frac{1}{\bar{E}_{xy}} = \frac{1}{E_{xy(0)}^{(n+1/2)}} + \sum_{(\mu)=1}^K \frac{1-\lambda_{(\mu)}}{E_{xy(\mu)}^{(n+1/2)}} \quad (56)$$

(5). Creep deformation for stress σ_{xz}

The equation for calculating the creep deformation is

$$\Delta\epsilon_{xz} = C_{xz}\Delta\sigma_{xz}\left(\frac{1}{E_{xz(0)}^{(n+1/2)}} + \sum_{(\mu)=1}^K \frac{1-\lambda_{(\mu)}}{E_{xz(\mu)}^{(n+1/2)}}\right) + \sum_{(\mu)=0}^K (1-\beta_{(\mu)})\gamma_{xz(\mu)}^{(n)} \quad (57)$$

where the subscript xz refers to the variable for this loading path. The updates of the internal variable and effective compliance are

$$\gamma_{xz(\mu)}^{(n+1)} = \frac{\lambda_{(\mu)}}{E_{xz(\mu)}^{(n+1/2)}} D_{xz}(\Delta\epsilon_{yy} - \Delta\epsilon_{yy}'') \bar{E}_{xz} + \beta_{(\mu)} \gamma_{xz(\mu)}^{(n)} \quad (58)$$

$$\frac{1}{\bar{E}_{xz}} = \frac{1}{E_{xz(0)}^{(n+1/2)}} + \sum_{(\mu)=1}^K \frac{1-\lambda_{(\mu)}}{E_{xz(\mu)}^{(n+1/2)}} \quad (59)$$

(6). Creep deformation for stress σ_{yz}

The equations for calculating the creep deformation and updating the effective compliance are the same as applying stress σ_{xz} , but the equation for updating the internal variable $\gamma_{xz(\mu)}^{(n+1)}$ should use $\Delta\epsilon_{yz}$ and $\Delta\epsilon_{yz}''$ rather than $\Delta\epsilon_{xz}$ and $\Delta\epsilon_{xz}''$, and so it is written as

$$\gamma_{xz(\mu)}^{(n+1)} = \frac{\lambda_{(\mu)}}{E_{xz(\mu)}^{(n+1/2)}} D_{xz}(\Delta\epsilon_{xx} - \Delta\epsilon_{xx}'') \bar{E}_{xz} + \beta_{(\mu)} \gamma_{xz(\mu)}^{(n)} \quad (60)$$

Let us now define the ratios between the effective stiffnesses at different loading paths:

$$r_1 = \bar{E}_y/\bar{E}_z \quad (61)$$

$$r_2 = \bar{E}_y/\bar{E}_{xz} \quad (62)$$

$$r_1 = \bar{E}_z/\bar{E}_{xz} \quad (63)$$

For a transversely isotropic material,

$$\bar{E}_{xy} = \frac{\bar{E}_y}{2(1+\nu_{xy})} \quad (64)$$

where ν_{xy} is the Poisson's ratio in the plane of isotropy.

Then, the components of the effective stiffness matrix C_{mn} can be written as

$$C_{mn} = \frac{1}{\bar{E}_z} C_z = \frac{1}{\bar{E}_y} C_y = \frac{1}{\bar{E}_{xy} C_{xy}} = \frac{1}{\bar{E}_{xz}} C_{xz} \quad (65)$$

$$C_{mn} = \bar{E}_z D_z = \bar{E}_y D_y = \bar{E}_{xy} D_{xy} = \bar{E}_{xz} D_{xz} \quad (66)$$

$$D_q = C_q^{-1} \quad q = z, y, xy, xz \quad (67)$$

The detailed formulations used to calculate C_q are given in Appendix I. Based on the method introduced above, the three-dimensional strain under a three-dimensional loading path can be calculated by superposition of Eq. (47) through Eq. (60).

4. Coupling between spherocylindrical microplane model and calculation method of anisotropic creep

As discussed in section 2, the task of the spherocylindrical microplane model is to define the following constitutive equation:

$$\Delta\sigma_{ij} = \bar{C}_{ijkl}\Delta\epsilon_{kl} \quad (68)$$

Eqs. (42), (45) and (46) give the effect of creep on the material stiffness matrix and the additional inelastic strain (Eq. (46)). To take creep into account, Eq. (68) should be rewritten as

$$\Delta\sigma_{kl} = \bar{C}_{ijkl}^{\text{eff}}(\Delta\epsilon_{ij} - \Delta\epsilon_{ij}'') \quad (69)$$

where $\bar{C}_{ijkl}^{\text{eff}}$ is the effective material stiffness matrix, which is calculated according to Eq. (65) or Eq. (66).

Instead of subdividing the cylindrical test specimens under unidirectional compressive load into 3D finite elements, we pursue here a simpler approximate analysis that assumes the cylinders to be in a uniform strain state. Thus, we merely need a point-wise solution of Eq. (69), coupling the spherocylindrical microplane model and the anisotropic creep calculation method. Eq. (69) does not require changing the numerical algorithm of the spherocylindrical microplane model described by Li et al.²⁴ Normally, in finite-element creep analysis with the microplane model,^{47,52} the microplane strain vector is the projection of the total strain tensor (creep included), but for the present simple point-wise estimation, we can project onto the microplane (Eqs. (2) and (3)) not the total strain tensor $\Delta\epsilon_{ij}$ but rather only the elastic part $\epsilon_{ij} - \Delta\epsilon_{ij}''$. Another difference from the elastic analysis is that the elastic parameters used in Eqs. 11–16 for calculating the microplane elastic moduli should be evaluated from the effective elastic parameters provided by Eq. (45).

Because the time-independent numerical algorithm for the spherocylindrical microplane model has been expounded in detail by Li et al.,²⁴ only the algorithm for calculating the macroscale effective elastic modulus and the creep strain induced by a constant load is described here, as follows:

1. For the initial time, i.e., $t = 0$, set the internal variables $\gamma_{\mu}^{(0)} = 0$.
2. Calculate the parameters of each Kelvin unit based on Eqs. 37–41.
3. For a finite loading step from $t = t_n$ to $t = t_{n+1}$, calculate $E_i^{(n+1/2)} = E_i(t_n + \Delta t/2)$ and the effective elastic parameters (Eqs. (49), (52), (56) and (59)).
4. According to Eqs. (47), (50), (53), (54), (57) and (60), calculate the creep produced by different constant stress tensor components.
5. Update the stress at the end of this loading step based on the numerical algorithm for the spherocylindrical microplane model.
6. Update the internal variables from $\gamma_{\mu}^{(n)}$ to internal variables $\gamma_{\mu}^{(n+1)}$ and return to step 2 until the calculation is finished.

5. Comparisons between experimental results and theoretical predictions

Creep tests of Longmaxi shale were conducted using an electro-hydraulic servo-controlled experimental apparatus for rock creep. The cylindrical specimens were prepared with a length of 100 mm and diameter of 50 mm. To investigate the effect of anisotropy on the creep characteristics of shale, four types of bedding layer orientations (Fig. 5), which are 0°, 45°, 75° and 90°, are used in the experiments. In each creep test, the confining pressure is first applied to reach 50 MPa and is then maintained for approximately 24 h; subsequently, different deviatoric stresses (20 MPa, 40 MPa, 60 MPa, 80 MPa, 100 MPa and 120 MPa) are applied to check the creep features of shale, as reported in Table 1. At each deviatoric stress level, the creep test time is approximately 48 h. Thus, the total test time for one creep test is approximately 13 days.

Fig. 6 depicts the primary experimental results of shale creep tests when the bedding layer orientations are different. As shown in the

Table 1
Experimental information of transversely isotropic creep tests.

Bedding layer orientations ($^{\circ}$)	Confining pressure (MPa)	Deviatoric stress (MPa)					
		1st	2nd	3rd	4th	5th	6th
0	50	20	40	60	80	100	120
45	50		60	80	120	~	~
75	50		60	80	120	~	~
90	50	20	40	60	80	100	120

figure, even when the deviatoric stress is as low as 20 MPa, creep exists when the bedding plane inclination angles are 0° and 90° . The creep strain becomes higher when the deviatoric stress increases. When the bedding layer orientation is 45° , the creep strain is greater than those of the specimens whose bedding layer orientations are 0° , 75° and 90° . The reason for this phenomenon is that the resistance to shear stress inclined at the 45° from the bedding plane is greater than those of the other three cases, as already explained in Section 3.1. The non-monotonic resistance to creep (and damage), being the weakest at an approximately 45° inclination, is a characteristic feature of shale that seems next to impossible to capture via tensorial constitutive models

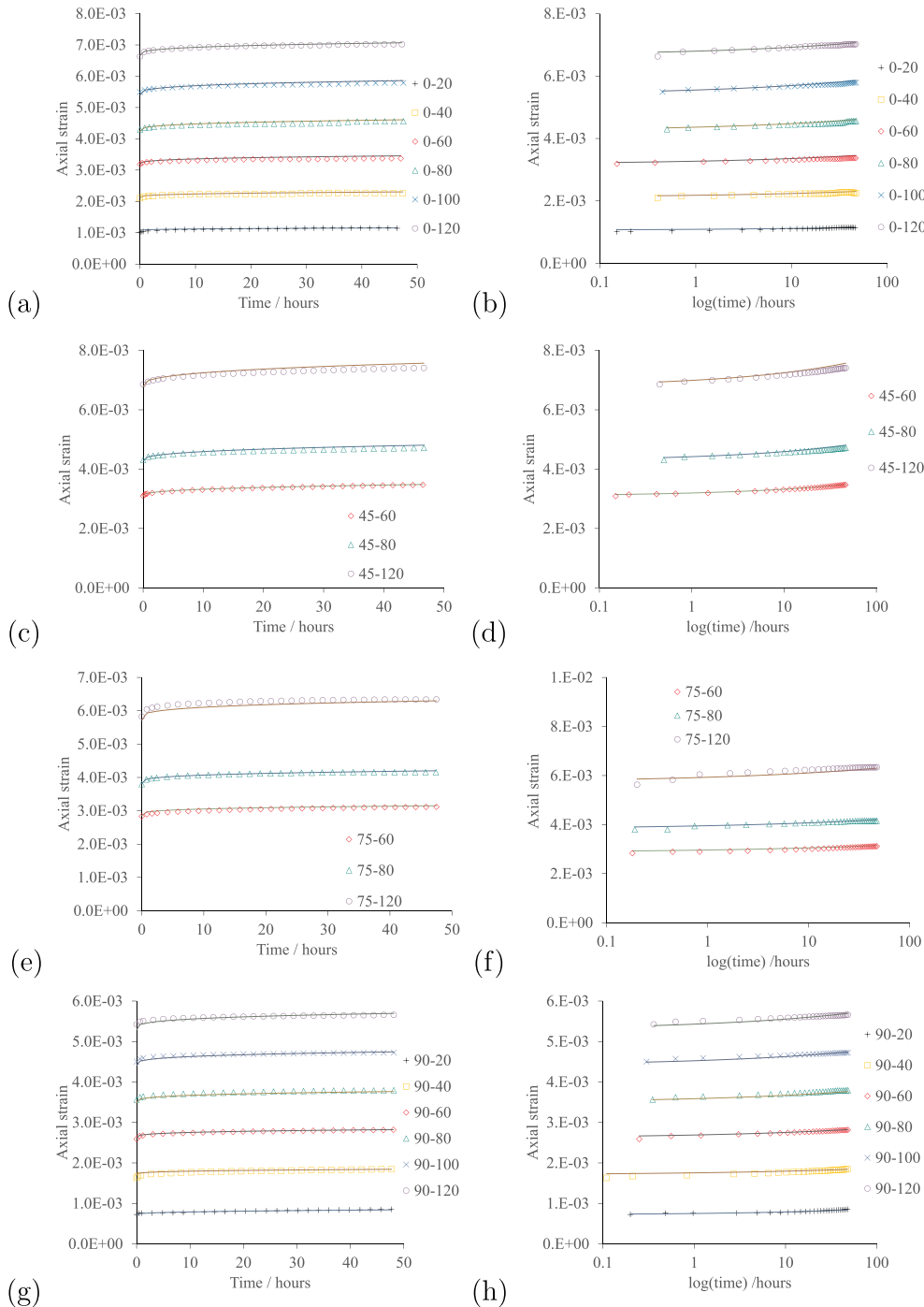


Fig. 6. Comparisons between theoretical prediction and anisotropic creep data for Longmaxi shale; the data in the left column are plotted on linear scales, while the data in the right column are plotted on logarithmic scales; (a) and (b) $\beta = 0^{\circ}$; (c) and (d) $\beta = 45^{\circ}$; (e) and (f) $\beta = 75^{\circ}$; (g) and (h) $\beta = 90^{\circ}$ (the solid lines and data points represent the simulation and experimental results, respectively).

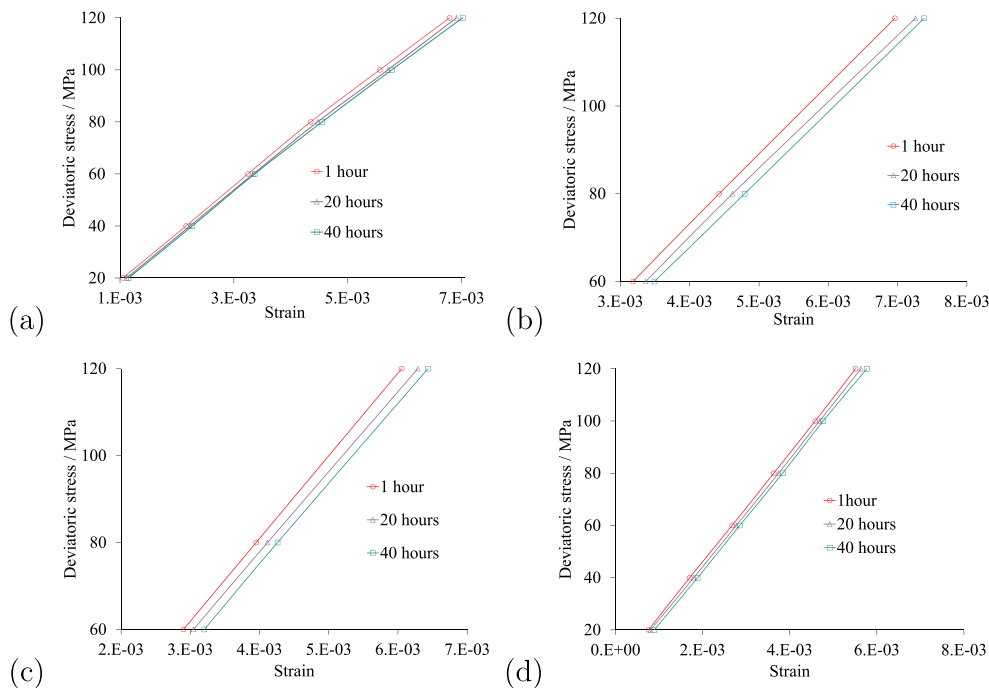


Fig. 7. Stress-strain isochrones of creep of shale under different bedding layer inclinations: (a) $\beta = 0^\circ$; (b) $\beta = 45^\circ$; (c) $\beta = 75^\circ$; (d) $\beta = 90^\circ$.

using stress invariants. At each deviatoric stress level, the creep rate decays similarly. This decay is independent of the bedding layer orientation, which means that Eq. (41) can be used even though the bedding orientation is different.

Fig. 7 presents the stress-strain isochrones of shale creep under different bedding layer orientations. The stress-strain isochrones demonstrate the linearity of the stress-strain relation of shale creep for deviatoric stresses up to 120 MPa, regardless of the bedding plane inclination. However, note that the strain magnitudes depend strongly on the bedding plane orientation.

To verify whether the present transversely isotropic creep model is sufficiently realistic, the model is implemented in a user's subroutine that is embedded in commercial software. The numerical simulation of creep tests for different bedding layer orientations is compared with the test results for transversely isotropic shale creep, as shown in Fig. 6. In these figures, the solid lines represent the simulation results, and the data points represent the experimental results. As can be observed from the figure, the theoretical model has the ability to capture the shale creep characteristics when the bedding plane inclination angle changes from 0° to 90° . When the bedding layer orientations are the same, the theoretical model can depict the strain evolution under different deviatoric stresses and at different times. Additionally, the model adequately captures, for anisotropic creep, the fact that the creep strain rate for the bedding layer orientation of 45° is the highest if the deviatoric stress and confining pressures are the same.

To provide a further validation, the creep test data for Tournemire argillite^{21,51} and anisotropic clay¹¹ are analyzed. Comparisons between the theoretical predictions and experimental data are presented in Fig. 8 and Fig. 9, in which the data are labeled by the bedding layer orientation and the deviatoric stress, such that, e.g., 0–20 means that the bedding layer orientation was 0° and the deviatoric stress was 20 MPa.

As shown in these figures, the present model is able to describe the primary creep characteristics of argillite and clay. It can also capture the anisotropic features of transversely isotropic creep satisfactorily. However, the proposed model cannot be expected to match closely the observed creep behaviors of argillite as the Longmaxi shale. The main reason is that the test data on the triaxial compression and direct

tension data of argillite used for calibrating the spherocylindrical microplane model are insufficient. Some parameters in the anisotropic model for predicting argillite creep are estimated from the experimental data for Longmaxi shale.

6. Creep regimes in hydraulic fracturing and scope limitation

The hydraulic fracturing and extraction of oil or gas proceeds on different time scales. One may thus distinguish three creep regimes:

1. The short-time creep up to several days in duration, which is relevant to the frac operation and hydraulic crack propagation. It affects the growth rate of hydraulic cracks and their opening during crack growth.
2. The medium-range creep, which is relevant to gas or oil extraction after fracking over a period from days to about 10 years. It affects the growth rate of hydraulic cracks at constant stress (probably similar to concrete⁷) and also governs the initial creep embedment of proppant grains and slow crack closing.
3. The creep on the geologic time span, which is crucial for the question whether the tectonic natural cracks in deep shale strata, formed over a period of 100–300 million years, could remain, at typical depth of 3 km, sufficiently open to enhance the overall gas permeability of shale stratum after fracking.⁴

The present and all previous laboratory experiments apply only to the short-time creep regime. This creep seems to be approximately linear viscoelastic, except at high stresses. Thus, the present model can be verified only for the short-time regime, although it should be possible to extend the applicability to the medium-range creep regime. No relevant data exist yet, although they could be obtained with the standard creep frames widely used for concrete.

Extension to the geologic time scale cannot be based on the present model. The creep of shale, like creep of all materials, eventually transits (at time called the Maxwell time⁴) from the primary creep to the secondary creep. The secondary creep represents an extremely slow steady-state viscous flow (under constant stress), devoid of memory but usually highly nonlinear in terms of stress. Some information about the

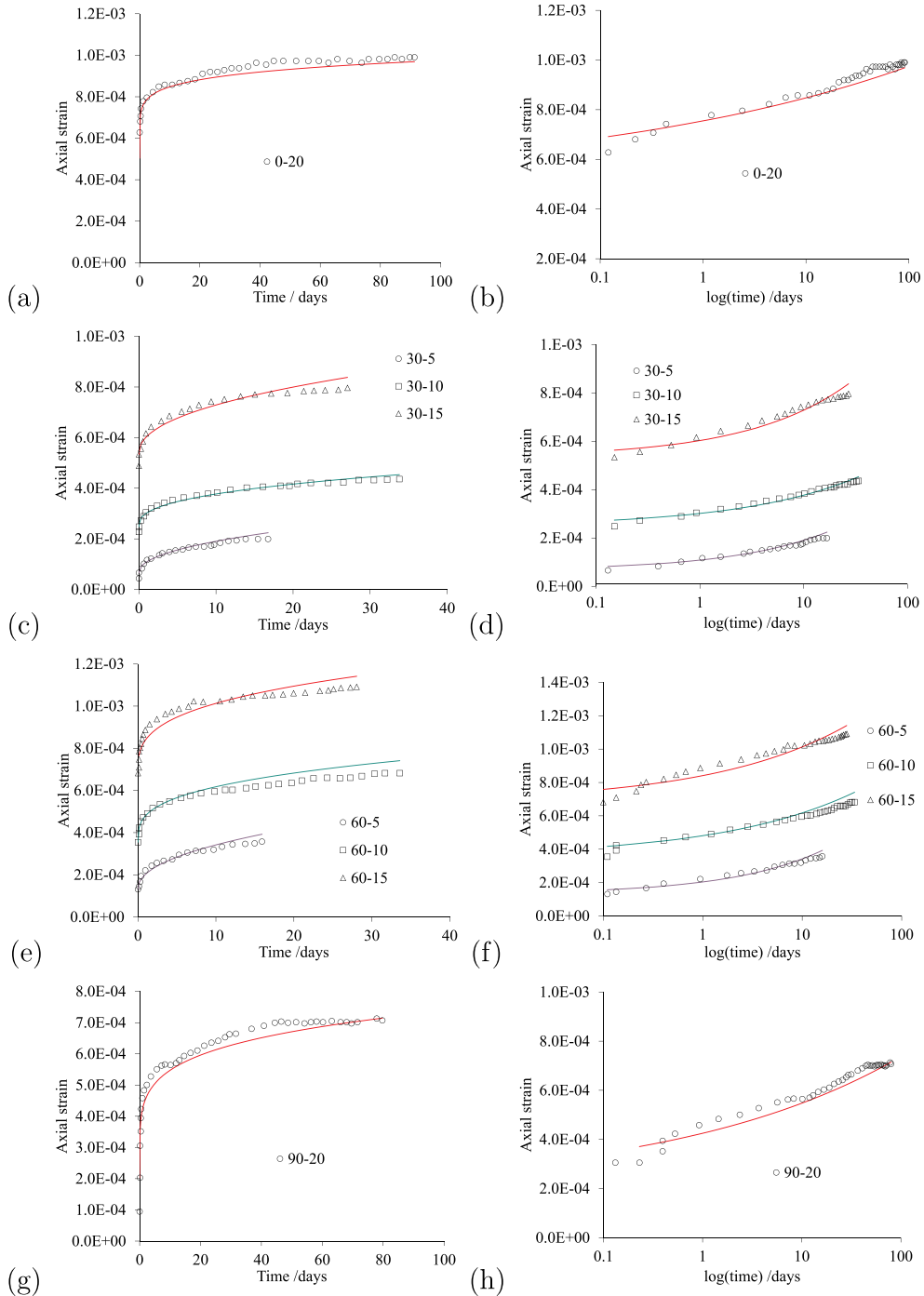


Fig. 8. Comparisons between theoretical prediction and anisotropic creep data for argillite: the data in the left column are plotted on linear scales, while the data in the right column are plotted on logarithmic scales; (a) and (b) $\beta = 0^\circ$; (c) and (d) $\beta = 45^\circ$; (e) and (f) $\beta = 60^\circ$; (g) and (h) $\beta = 90^\circ$ (the solid lines and data points represent the simulation and experimental results, respectively).

secondary creep of rocks has been inferred from geologic processes such as the postglacial rebound of upper mantle or lithosphere⁴ and could probably be also obtained from analysis of geologic strata folding.

7. Conclusions

- Similar to material damage, the creep accompanying damage tends to localize into distinct directions of slip on planes of distinct orientation. This feature, which could hardly be properly captured by tensorial macrocontinuum constitutive laws with tensorial invariants, can be captured easily by the microplane model, as

demonstrated here.

- The spherocylindrical microplane constitutive model, developed previously for time-independent deformations of shale, can be, and here is, successfully generalized for anisotropic creep effects. The model can reproduce not only the stress-induced incremental anisotropy but also the inherent material anisotropy.
- To set up the constitutive model, it helps to formulate first the creep for three elementary stress configurations: the creep caused by a principal stress component acting either (i) parallel or (ii) orthogonal to the bedding planes, and (iii) the creep due to shear stress parallel to the bedding planes, which is equivalent to the difference

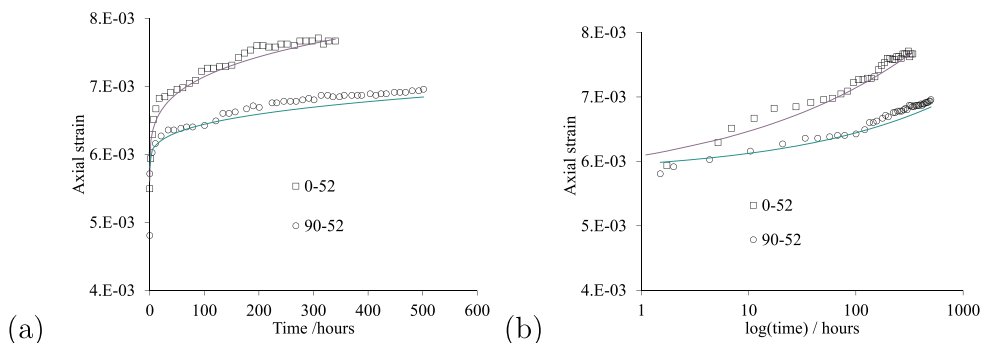


Fig. 9. Comparisons between theoretical prediction and anisotropic creep data for Barnett shale: the data in the left column are plotted on linear scales, while the data in the right column are plotted on logarithmic scales (the solid lines and data points represent the simulation and experimental results, respectively).

of principal stresses at 45° inclinations to the bedding planes. Combining these three elementary cases leads to a general creep constitutive model for anisotropic shale.

4. The Kelvin chain parameters in the present creep extension of anisotropic microplane model are effectively identified on the basis of a continuous retardation spectrum. All the values of the dashpot viscosities and spring stiffnesses can thus be identified.
5. Short-time creep tests of shale (of two-day duration) are conducted and used to calibrate the model. They demonstrate linear dependence of the creep strain on the stress. Comparisons of the experimental results and numerical predictions show that the proposed linear creep model can simulate the main features of the anisotropic

creep behavior of shale and other geomaterials.

Acknowledgments

The first author wishes to acknowledge financial support from the National Natural Science Foundation of China (No. 51804203), the Department of Science and Technology of Sichuan Province (No. 2017HH0005), and Sichuan University (No. 0060304153002, No. 20826041C4082). Experience from prior studies partially supported by the U.S. Department of Energy through subcontract No. 37008 of Northwestern University with Los Alamos National Laboratory was very helpful for the present research.

Appendix. Calculation of elasticity matrices C_m in Eq. (65)

Matrices C_m , in which m can represent z , y , xy , xz , are calculated as follows:

$$C_z = \begin{bmatrix} 1/r_1 & -\nu_{xy}/r_1 & -\nu_{xz} & 0 & 0 & 0 \\ -\nu_{xy}/r_1 & 1/r_1 & -\nu_{xz} & 0 & 0 & 0 \\ -\nu_{xz} & -\nu_{xy} & 1 & 0 & 0 & 0 \\ 0 & 0 & 0 & 2(1 + \nu_{xy})/r_1 & 0 & 0 \\ 0 & 0 & 0 & 0 & r_3 & 0 \\ 0 & 0 & 0 & 0 & 0 & r_3 \end{bmatrix} \quad (70)$$

$$C_y = \begin{bmatrix} 1 & -\nu_{xy} & -\nu_{xz} & 0 & 0 & 0 \\ \nu_{xy} & 1 & -\nu_{xz} & 0 & 0 & 0 \\ -\nu_{xz} & -\nu_{xy} & r_1 & 0 & 0 & 0 \\ 0 & 0 & 0 & 2(1 + \nu_{xy}) & 0 & 0 \\ 0 & 0 & 0 & 0 & r_2 & 0 \\ 0 & 0 & 0 & 0 & 0 & r_2 \end{bmatrix} \quad (71)$$

$$C_{xy} = \begin{bmatrix} 1/r_2 & \nu_{xy}/r_2 & -\nu_{xz}/r_2 & 0 & 0 & 0 \\ \nu_{xy}/r_2 & 1/r_2 & -\nu_{xz}/r_2 & 0 & 0 & 0 \\ -\nu_{xz}/r_2 & -\nu_{xy}/r_2 & 1/r_3 & 0 & 0 & 0 \\ 0 & 0 & 0 & 2(1 + \nu_{xy})/r_2 & 0 & 0 \\ 0 & 0 & 0 & 0 & 1 & 0 \\ 0 & 0 & 0 & 0 & 0 & 1 \end{bmatrix} \quad (72)$$

$$C_{xz} = \frac{1}{2(1 + \nu_{xy})} \begin{bmatrix} 1 & -\nu_{xy} & -\nu_{xz} & 0 & 0 & 0 \\ \nu_{xy} & 1 & -\nu_{xz} & 0 & 0 & 0 \\ -\nu_{xz} & -\nu_{xy} & r_1 & 0 & 0 & 0 \\ 0 & 0 & 0 & 2(1 + \nu_{xy}) & 0 & 0 \\ 0 & 0 & 0 & 0 & r_2 & 0 \\ 0 & 0 & 0 & 0 & 0 & r_2 \end{bmatrix} \quad (73)$$

Appendix A. Supplementary data

Supplementary data to this article can be found online at <https://doi.org/10.1016/j.ijrmms.2019.104074>.

References

1. Beckwith R. Hydraulic fracturing: the fuss, the facts, the future. *J Pet Technol*. 2010;62(12):34–40.
2. Asala H, Ahmadi M, Taleghani AD. Why re-fracturing works and under what conditions. *SPE Annual Technical Conference and Exhibition*. Society of Petroleum Engineers; 2016.
3. Bažant ZP, Salvato M, Chau VT, et al. Why fracking works. *J Appl Mech*. 2014;81(10):101010.
4. Chau VT, Li CB, Rahimi-Aghdam S, Bažant ZP. The enigma of large-scale permeability of gas shale: preexisting or frac-induced? *J Appl Mech*. 2017;84(6):061008.
5. Chhatre SS, Braun EM, Simha S, et al. Steady-state stress-dependent permeability measurements of tight oil-bearing rocks. *Petrophysics*. 2015;56(02):116–124.
6. Xie H, Gao F, Ju Y, et al. Novel idea of the theory and application of 3d volume fracturing for stimulation of shale gas reservoirs. *Chin Sci Bull*. 2016;61(1):36–46.
7. Bažant ZP, Li YN. Cohesive crack with rate-dependent opening and viscoelasticity: I. mathematical model and scaling. *Int J Fract*. 1997;86(3):247–265.
8. Sone H. *Mechanical Properties of Shale Gas Reservoir Rocks, and its Relation to the In-Situ Stress Variation Observed in Shale Gas Reservoirs* Stanford University; 2012 PhD thesis.
9. Sone H, Zoback MD. Time-dependent deformation of shale gas reservoir rocks and its long-term effect on the in situ state of stress. *Int J Rock Mech Min Sci*. 2014;69:120–132.
10. Abdi H, Evgin E. *Laboratory Characterization, Modeling, and Numerical Simulation of an Excavation Damaged Zone Around Deep Geologic Repositories in Sedimentary Rocks*. Final report for Canadian Nuclear Safety Commission; 2013.
11. Liu Z, Xie S, Shao JF, et al. Effects of deviatoric stress and structural anisotropy on compressive creep behavior of a clayey rock. *Appl Clay Sci*. 2015;114:491–496.
12. Zhang XP, Wong LNY, Wang SJ, et al. Engineering properties of quartz mica schist. *Eng Geol*. 2011;121(3):135–149.
13. Fabre G, Peltier F. Creep and time-dependent damage in argillaceous rocks. *Int J Rock Mech Min Sci*. 2006;43(6):950–960.
14. Villamor Lora R, Ghazanfari E. Creep behavior of shale formations in shale gas development. *IFCEE*. 2015:2024–2033.
15. Rassouli F, Zoback M. A Comparison of Short-Term and Long-Term Creep Experiments in Unconventional Reservoir Formations. *The 50th US Rock Mechanics/Geomechanics Symposium*. 2016; 2016 ARMA-2016-430.
16. Li Y, Ghassemi A. Creep behavior of Barnett, Haynesville, and marcellus shale. *46th US Rock Mechanics/Geomechanics Symposium*. 2012; 2012 ARMA-2012-330.
17. Almasoodi MM, Abousleiman YN, Hoang SK. Viscoelastic creep of eagle ford shale: investigating fluid-shale interaction. *SPE/CSUR Unconventional Resources Conference-Canada*. 2014; 2014.
18. Yang SQ, Cheng L. Non-stationary and nonlinear visco-elastic shear creep model for shale. *Int J Rock Mech Min Sci*. 2011;48(6):1011–1020.
19. Nedjar B, Le Roy R. An approach to the modeling of viscoelastic damage. application to the long-term creep of gypsum rock materials. *Int J Numer Anal Methods Geomech*. 2013;37(9):1066–1078.
20. Nguyen T, Nguyen S, Vu M, et al. Effective viscoelastic properties of micro-cracked heterogeneous materials. *Int J Damage Mech*. 2016;25(4):557–573.
21. Rouabhi A, Tijani M, Rejeb A. Triaxial behaviour of transversely isotropic materials: application to sedimentary rocks[J]. *Int J Numer Anal Methods Geomech*. 2007;31(13):1517–1535.
22. Leoni M, Karstunen M, Vermeer P. Anisotropic creep model for soft soils. *Geotechnique*. 2008;58(3):215–226.
23. Shao JF, Chau K, Feng X. Modeling of anisotropic damage and creep deformation in brittle rocks. *Int J Rock Mech Min Sci*. 2006;43(4):582–592.
24. Li CB, Bažant ZP, Caner FC, et al. Spherocylindrical microplane constitutive model for shale and other anisotropic rocks. *J Mech Phys Solids*. 2017;103:155–178.
25. Bažant ZP, Oh BH. Microplane model for progressive fracture of concrete and rock. *J Eng Mech*. 1985;111(4):559–582.
26. Bažant ZP, Prat PC. Microplane model for brittle-plastic material: I. Theory. *J Eng Mech*. 1988;114(10):1672–1688.
27. Bažant ZP, Xiang YY, Prat PC. Microplane model for concrete. i: stress-strain boundaries and finite strain. *J Eng Mech*. 1996;122(3):245–254 1996.
28. Bažant ZP, Caner FC, Carol I, et al. Microplane model M4 for concrete. I: formulation with work-conjugate deviatoric stress. *J Eng Mech*. 2000;126(9):944–953.
29. Bažant ZP, Caner FC. Microplane model M5 with kinematic and static constraints for concrete fracture and anelasticity. I: Theory. *J Eng Mech*. 2005;131(1):31–40.
30. Caner FC, Bažant ZP. Microplane model M7 for plain concrete. I: Formulation *J Eng Mech*. 2013;139(12):1714–1723.
31. Bažant ZP, Zi G. Microplane constitutive model for porous isotropic rocks. *Int J Numer Anal Methods Geomech*. 2003;27(1):25–47.
32. Brocca Michele, Bažant ZP. Microplane constitutive model and metal plasticity. *Appl Mech Rev*. 2000;53(10):265–281.
33. Jin W, Arson C. Anisotropic nonlocal damage model for materials with intrinsic transverse isotropy. *Int J Solids Struct*; 139:29–42.
34. Jin W, Arson C. Fluid-driven transition from damage to fracture in anisotropic porous media: a multi-scale XFEM approach. *Acta Geotechnica*. 2019 <https://doi.org/10.1007/s11440-019-00813-x>.
35. Bažant ZP, Ozaydin IK, Krizek RJ. Micromechanics model for creep of anisotropic clay. *J Eng Mech Div, Am Soc Civil Eng*. 1975;101:57–78.
36. Bažant ZP, Kim JK. Creep of anisotropic clay: microplane model. *J Geotech Eng ASCE*. 1986;112(4):458–475.
37. Brocca M, Bažant ZP, Daniel IM. Microplane model for stiff foams and finite element analysis of sandwich failure by core indentation. *Int J Solids Struct*. 2001;38:8111–8132.
38. Jin Cr, Salvato M, Li WX, et al. Elastic microplane formulation for transversely isotropic materials. *J Appl Mech*. 2017;84(1):011001.
39. Cusatis G, Beghini H, Bažant ZP. Spectral stiffness microplane model for quasi-brittle composite laminates: I. Theory *J Appl Mech ASME*. 2008;75(1):021009.
40. Salvato M, Ashari SE, Cusatis G. Spectral stiffness microplane model for damage and fracture of textile composites. *Compos Struct*. 2016;137:170–184.
41. Kirane K, Salvato M, Bažant ZP. Microplane-triad model for elastic and fracturing behavior of woven composites. *J Appl Mech ASME*. 2016;83(4):041006.
43. Bažant ZP. Numerically stable algorithm with increasing time steps for integral-type aging creep. *Proc., 1st International Conf. On Structural Mechanics in Reactor Technology*. 1971; 1971.
44. Guindon L. Viscoelastic creep of eagle ford shale: investigating fluid/shale interaction. *J Can Pet Technol*. 2015;54(3):142–143.
45. Chen WL, Kulatilake P. Creep behavior modeling of a marble under uniaxial compression. *Geotech Geol Eng*. 2015;33(5):1183–1191.
46. Fahimifar A, Karami M, Fahimifar A. Modifications to an elasto-visco-plastic constitutive model for prediction of creep deformation of rock samples. *Soils Found*. 2015;55(6):1364–1371.
47. Bažant ZP, Jirásek M. *Creep and Hygrothermal Effects in Concrete Structures*. Springer; 2018.
48. Tschoegl NW. A general method for the determination of approximations to the spectral distributions from the dynamic response functions. *Rheol Acta*. 1973;12(1):82–83.
49. Bažant ZP, Xi Y. Continuous retardation spectrum for solidification theory of concrete creep. *J Eng Mech*. 1995;121(2):281–288.
50. Jirásek M, Bažant ZP. *Inelastic Analysis of Structures*. John Wiley & Sons; 2002.
51. Rejeb A. *Time-dependent Behaviour of Tournemire Argillites (France)*. 10th ISRM Congress. International Society for Rock Mechanics; 2003.
52. Bažant ZP, Yu Q, Li GH. Excessive long-time deflections of prestressed box girders. II: numerical analysis and lessons learned. *J Struct Eng*. 2012;138(6):687–696.